

Linear Stability of Hypersonic Flow over a Parabolic Leading Edge

Sean Hu *and Xiaolin Zhong †

University of California, Los Angeles, California 90095

Abstract

The stability of the hypersonic flow over a parabolic leading edge is numerically investigated using linear stability analysis accounting for the existence of shock waves in comparison with direct numerical simulations. The linear stability analysis is performed using a global spectral collocation method accounting for the shock effects by using Rankine-Hugoniot shock conditions on the upper boundary. It is shown that in addition to the boundary layer first modes and higher modes (Mack modes), the linear stability of the hypersonic flow between a bow shock and a parabolic leading edge has a new family of modes, shock modes. The shock modes are important mainly in the shock layer. Due to the bow shock at the upper boundary, disturbance modes can communicate between the shock layer and the boundary layer. As a consequence, the evolution of boundary layer modes in the flow field may deviate from that in a flat plate boundary layer case. The stability characteristics of these modes are studied including the effects of frequency, Reynolds number, wave angle.

1 Introduction

The prediction of stability and transition of hypersonic flows is critical to the accurate calculations of aerodynamic forces and heating rates for hypersonic vehicles. For hypersonic flow over blunt bodies, many factors, such as bow shocks, surface curvature, entropy layer, nose bluntness, and real gas effects, influence the characteristics of hypersonic flow instability. Early experimental results on hypersonic transition include the work by Kendall [7] and Demetriades [8]. Stetson et al. [9] investigated the stability of the laminar boundary layer on a blunt, 7-degree half angle cone at $M_\infty = 8$ experimentally. It was found that small nosetip bluntness make significant changes in the stability character-

istics of the boundary layer comparing to sharp cone. Namely, the critical Reynolds number in the case with small bluntness is found to be much higher than the case with a sharp cone. They also found that disturbances grow outside the boundary layer, in the entropy layer, indicating the existence of an inviscid instability. A series of theoretical and numerical work were conducted on the supersonic and hypersonic instability problems in comparison with the experimental results. Reshotko et al. [11] used a multiple scales method to analyze the spatial stability of a laminar supersonic flow over a blunt plate. Cowley et al. [49] investigated the instability of a compressible flow past a wedge in the hypersonic limit using asymptotic analysis. Several authors [10] [12] [13] [54] compared numerical linear stability results with Stetson's experimental results. They showed qualitative agreement with the experimental results. However, the spatial amplification rates of the second modes resolved by numerical approaches show much higher maxima than the experimental results. Kufner et al. [12] studied the effects of mean flow variations on the instability of hypersonic flow past blunt cones in resolving the discrepancies in the amplification rate. They found that the discrepancies were not due to the use of different mean flow solutions. Indeed, the discrepancies may due to the known limitations of the theoretical and numerical linear stability approaches as well as inaccurate main flow solutions.

Recently, direct numerical simulations (DNS) of hypersonic flow over a parabolic leading edge including the effects of boundary layers and shock layers were conducted by Zhong [39] who studied the generation of instability waves due to freestream acoustic disturbances for a two-dimensional Mach 15 flow over a parabola by numerically solving full Navier-Stokes equations using a new explicit fifth-order shock fitting upwind scheme. Better understanding of the stability characteristics of the hypersonic parabolic body flow can be achieved if the overall wave phenomena from DNS can be decomposed into linear and non-linear parts, and the effects of the shock wave, curvature, and three-dimensional waves can be identified. The numerical linear stability tools have the flexibility to study the effects of curvature, shock boundary conditions, as well as wave angles. A comparison between the DNS and the linear stability (LST) results may provide in-

*Graduate Student, seanh@seas.ucla.edu

†Assistant Professor, Mechanical and Aerospace Engineering Department, Member AIAA

sights to the stability characteristics of the flow.

Since the flow of interest is confined between the body surface and the bow shock, it is expected that both boundaries will affect the stability characteristics. The effects of the shock boundary conditions were evident from the DNS results^[38] Most of the research done before regarding the linear stability of the compressible flows, however, ignored the presence of a shock and used free stream (homogeneous) conditions at the far field or the asymptotic conditions just outside the boundary layer. For the hypersonic parabolic body case where important wave phenomena are observed between the viscous boundary layer and the shock, shock plays a vital role and introduces additional flow features such as entropy layer to the flow. It is therefore reasonable to use appropriate shock boundary conditions instead for stability analysis.

It is known that there exist wave interactions among the shock wave, boundary-layer originated instability waves and the free stream disturbances for hypersonic flow instability. The theoretical approach in analyzing the problem was developed by Ribner^[44] and McKenzie *et al.*^[45] Anyiwo *et al.*^[46] used this approach in analyzing the turbulence amplifications in the shock wave/boundary layer interaction. The main result of this theory is that the interaction of any mode, for instance, an acoustic wave with a shock wave, produces all three modes, a acoustic mode, a vorticity mode and a entropy mode. More recent approach of solving the problem involves direct numerical simulations. Zang *et al.*^[47] examined the interaction of plane waves with shocks using the DNS approach and confirmed the linear theory results. In the aforementioned investigations, disturbances were considered to originate ahead of the shock. In the hypersonic parabolic body case, however, the disturbances come from behind the shock. The first attempt to study the effects of a shock on the boundary layer stability was probably Petrov's work^[48]. In solving the compressible boundary layer linear stability problem, he replaced the inviscid asymptotic eigensolution outside the boundary layer by the linearized steady Rankine-Hugoniot condition for the normal momentum equation as the shock boundary condition. In doing so, he obtained solutions for a two-dimensional flow over a wedge in the hypersonic limit. The triple-deck theory was used by Cowley *et al.*^[49] along with the linearized Rankine-Hugoniot conditions to investigate the influence of a shock on the stability of boundary layer flow over a wedge. A key result obtained was that the presence of a shock allows more than one unstable viscous mode for relatively small ranges of frequency.

Chang *et al.*^[43] started from the unsteady Rankine-

Hugoniot conditions to obtain a set of perturbation equations accounting for the effect of shock velocity due to the perturbed wave originated from inside the boundary layer. This set of equations were then imposed as boundary conditions at the shock for the quasi-parallel linearized stability equations for compressible flows. They used a multidomain spectral method and a fourth order compact difference scheme to solve the stability equations. Their results showed that the shock has little effect on the boundary layer stability (subsonic first and second mode disturbances) when the shock is located outside the boundary layer edge. The presence of the shock induces unstable supersonic modes at finite Reynolds numbers which have oscillatory structure between the boundary layer and shock. When the shock is sufficiently close to the boundary layer edge, the shock influences the wave modes with finite disturbance amplitude near the shock. Stuckert^[53] used similar approach as above in solving the linear stability problem for hypersonic flow over a sharp cone.

This paper studies the linear stability of hypersonic flow over a parabolic body in conjunction with DNS simulation. In the present study, the formulations of the temporal and spatial linear stability equations followed Malik^[37] closely. While we use both the fourth-order finite-difference method and the spectral collocation method in our stability calculations, the results for the spatial hypersonic parabolic body problem are mostly obtained using the spectral collocation method. Shock jump conditions are enforced following the formulation by Chang *et al.*^[43] closely. To better approximate the physical conditions in the hypersonic parabolic body problem, in addition to the shock jump conditions, the basic flow normal velocity (V) terms are not neglected in the linear stability analysis. Linear stability results with shock jump condition for the hypersonic parabolic body problem are then presented along with DNS results with a focus on the fundamental wave phenomena. The stability characteristics of the important modes in the flow field are also discussed.

2 Formulation

A. Equations

The linear stability is considered for compressible viscous flow confined between two boundaries located at $y^* = 0$ (lower boundary) and $y^* = L^*$ (upper boundary), where the superscript "*" represents dimensional quantities. In the Cartesian coordinates, the x^* , y^* , z^* coordinates are those in the stream wise, wall-normal,

and spanwise directions respectively. The gas is assumed to be a perfect Newtonian gas. The flow variables at the upper boundary (just behind the shock) are denoted by a subscript “e”. In the case of hypersonic flow over parabolic body, the upper boundary is the shock wave, while the lower boundary is the body surface. The temperatures and velocities at the boundaries were computed together with the basic flow profiles. The three-dimensional Navier-Stokes equations are:

$$\rho^* \left[\frac{\partial \mathbf{u}^*}{\partial t^*} + \mathbf{u}^* \cdot \nabla \mathbf{u}^* \right] = -\nabla p^* + \nabla \cdot [\lambda^* (\nabla \cdot \mathbf{u}^*) \mathbf{I} + \mu^* (\nabla \mathbf{u}^* + \nabla \mathbf{u}^{*tr})], \quad (1)$$

$$\frac{\partial \rho^*}{\partial t^*} + \nabla \cdot (\rho^* \mathbf{u}^*) = 0, \quad (2)$$

$$\rho^* c_p^* \left[\frac{\partial T^*}{\partial t^*} + \mathbf{u}^* \cdot \nabla T^* \right] = \nabla \cdot (k^* \nabla T^*) + \frac{\partial p^*}{\partial t^*} + \mathbf{u}^* \cdot \nabla \mathbf{u}^* + \Phi^*, \quad (3)$$

$$p^* = \rho^* R^* T^*, \quad (4)$$

where \mathbf{u}^* is the velocity vector, ρ^* is the density, p^* is the pressure, T^* is the temperature, R^* is the gas constant, c_p^* is the specific heat at constant pressure, k^* is the thermal conductivity, μ^* is the first coefficient of viscosity, and λ^* is the second coefficient of viscosity. The viscous dissipation function, Φ^* , is given as

$$\Phi^* = \lambda^* (\nabla \cdot \mathbf{u}^*)^2 + \frac{\mu^*}{2} [\nabla \mathbf{u}^* + \nabla \mathbf{u}^{*tr}]^2. \quad (5)$$

The flow variables and equations are non-dimensionalized as follows: velocities by U_e^* , length scales by L_e^* (local shock distance), density by ρ_e^* , temperature by T_e^* , pressure by $\rho_e^* U_e^{*2}$, and time scale by L^*/U_e^* . All other variables are nondimensionalized by their corresponding values on the upper boundary. The dimensionless variables are represented by the same symbols as those used for the dimensional variables but without the superscript “*”. The Reynolds number is defined as

$$Re = \frac{U_e^* \rho_e^* L^*}{\mu_e^*}, \quad (6)$$

and the Mach number is

$$M_e = \frac{U_e^*}{(\gamma R^* T_e^*)^{1/2}}, \quad (7)$$

where $R^* = c_p^* - c_v^*$, c_v^* is the specific heat at constant volume, and γ is the ratio of specific heats. The Prandtl number is defined as $Pr = \mu^* c_p^*/k^*$. The viscosity coefficient is determined by Sutherland’s law,

$$\mu = T^{1.5} \left(\frac{1+C}{T+C} \right), \quad (8)$$

where C is a constant. In this paper, it is assumed that $C = 110.33/T_e$ for the parabolic body hypersonic flow, where T_e is the temperature just behind the shock, $\lambda = -2/3\mu$, $\gamma = 1.4$, and $Pr = 0.72$.

B. Basic flow solutions

Basic flow solutions for the hypersonic flow over a parabolic leading edge was obtained by Zhong^[38] by using the new high-order shock-fitting scheme. Note that the DNS and the linear stability analysis share the same high-accuracy basic flow solutions. Since the wave patterns are quite complex both close to the wall and to the shock, a natural choice of stretching function for the linear stability analysis is a cosine function. The basic flow at the collocation points are then obtained by using a high order interpolation scheme.

C. Linear stability equations

The linear stability analysis is based on a normal mode analysis of the linearized perturbation equations of the three-dimensional Navier-Stokes equations. The LST formulas presented in this paper are for general compressible flows with parallel steady flow fields. The perturbation equations are derived by representing the instantaneous flow variables as a sum of a basic flow solution and a small fluctuation quantity, i.e.

$$\begin{aligned} u &= \bar{U}(y) + u'(x, y, z, t) \\ v &= \bar{V}(y) + v'(x, y, z, t) \\ w &= \bar{w}'(x, y, z, t) \\ p &= \bar{p} + p'(x, y, z, t) \\ T &= \bar{T}(y) + T'(x, y, z, t) \end{aligned} \quad (9)$$

Substituting Eq. (9) into the nondimensional form of the governing Eqs. (1)–(5), and dropping the nonlinear and high-order terms yield a set of linear differential equations for the perturbation variables. Details of the linear perturbation equations and other formulations can be found in Malik.^[37] In the normal mode analysis for the linear disturbances, the fluctuations of flow quantities are assumed to be represented by harmonic

waves of the following form:

$$[u', v', p', T', w']^{tr} = [\hat{u}(y), \hat{v}(y), \hat{p}(y), \hat{T}(y), \hat{w}(y)]^{tr} e^{i(\alpha x + \beta z - \omega t)}, \quad (10)$$

where α and β are the wavenumbers in x and z directions respectively, and ω is the frequency of the disturbance waves. These parameters are in general complex numbers. The complex amplitude (eigen) function of a typical flow variable, say u , is $\hat{u}(y)$. Substituting Eq. (10) into the linearized perturbation equations leads to a homogeneous system of ordinary differential equations:

$$(\mathbf{A} D^2 + \mathbf{B} D + \mathbf{C}) \Phi = 0, \quad (11)$$

where D is the derivative operator in y direction, i.e., $D = d/dy$ and $D^2 = d^2/dy^2$. In the equation above, Φ is a vector defined as

$$\Phi = \begin{bmatrix} \hat{u}(y) \\ \hat{v}(y) \\ \hat{p}(y) \\ \hat{T}(y) \\ \hat{w}(y) \end{bmatrix}, \quad (12)$$

and \mathbf{A} , \mathbf{B} and \mathbf{C} , which are 5×5 matrices, are functions of α , β , ω , Re , M_∞ , and the basic flow solutions. The detailed expressions of matrices \mathbf{A} , \mathbf{B} and \mathbf{C} can be found in Ref. [37], and they are not repeated here. In solving the linear stability problem for the hypersonic parabolic body case, where the normal direction basic flow velocity V is not very small comparing to U , it is reasonable to add the terms with V ignored by the parallel assumption back to matrices \mathbf{A} , \mathbf{B} and \mathbf{C} . These extra terms will be given in Appendix.

D. Linear stability boundary conditions

In hypersonic boundary layer stability problems, no-slip conditions apply at the body surface, i.e.,

$$\hat{u}(0) = \hat{v}(0) = \hat{w}(0) = \hat{T}(0) = 0. \quad (13)$$

At the bow shock, shock conditions must hold. We followed the derivations from Chang^[43] closely. The formulation is given in the following for completeness. For a shock given by $y_0 = f(x, z, t)$ with the time averaged shock position $\bar{y}_0 = \bar{f}(x)$ and the local shock

slope $a = \tan\theta = d\bar{f}/dx$, the jump conditions across the shock are:

$$\frac{\partial f}{\partial t}[Q] + \frac{\partial f}{\partial x}[E] - [F] + \frac{\partial f}{\partial z}[G] = 0. \quad (14)$$

Vectors Q, E, F, G are defined by

$$\begin{aligned} Q &= (\rho, \rho u, \rho v, \rho w, e)^{tr} \\ E &= (\rho u, \rho u^2 + p, \rho uv, \rho uw, (e+p)u)^{tr} \\ F &= (\rho v, \rho uv, \rho v^2 + p, \rho vw, (e+p)v)^{tr} \\ G &= (\rho w, \rho uw, \rho vw, \rho w^2 + p, (e+p)w)^{tr} \end{aligned} \quad (15)$$

where

$$e = \frac{p}{\gamma - 1} + \frac{1}{2}\rho(u^2 + v^2 + w^2). \quad (16)$$

The jump of any quantity ϕ across the shock is denoted by

$$[\phi] = \phi_1 - \phi_2 \quad (17)$$

where the subscripts 1 and 2 denotes the conditions ahead and behind the shock wave, respectively. Equation (15) is the unsteady Rankine-Hugoniot condition which governs the unsteady motion of a shock wave. The position function of the shock can be perturbed according to

$$f = \bar{f} + f'. \quad (18)$$

We assume that Eq. (15) is valid at $y = \bar{f}$ since for small disturbances $|f'| \ll |\bar{f}|$. We also assume there is no disturbances ahead of the shock. The disturbances in the boundary layer or shock layer can not penetrate through the shock because the flow is supersonic outside the shock layer. A normal mode analysis to Eq(15) leads to

$$i(\alpha[\bar{E}] + \beta[\bar{G}] - \omega[\bar{Q}])\hat{f} + a[\hat{E}] - [\hat{F}] = 0 \quad (19)$$

where harmonic wave forms are used in consistency with the linear stability equations

$$[f', \rho', u', v', p', T', w']^{tr} = [\hat{f}, \hat{\rho}, \hat{u}(y), \hat{v}(y), \hat{p}(y), \hat{T}(y), \hat{w}(y)]^{tr} e^{i(\alpha x + \beta z - \omega t)}, \quad (20)$$

and the vectors $[\hat{E}]$ and $[\hat{F}]$ are

$$[\hat{E}] = \begin{bmatrix} \rho_2 \hat{u} + \hat{\rho} u_2 \\ \hat{\rho} u_2^2 + 2\rho_2 u_2 \hat{u} + \hat{p} \\ \hat{\rho} u_2 v_2 + \rho_2 \hat{u} v_2 + \rho_2 u_2 \hat{v} \\ \hat{\rho} u_2 w_2 + \rho_2 \hat{u} w_2 + \rho_2 u_2 \hat{w} \\ (e_2 + p_2) \hat{u} + u_2 (\hat{e} + \hat{p}) \end{bmatrix}, \quad (21)$$

$$[\hat{F}] = \begin{bmatrix} \rho_2 \hat{v} + \hat{\rho} v_2 \\ \hat{\rho} v_2^2 + 2\rho_2 v_2 \hat{v} + \rho_2 u_2 \hat{v} \\ \hat{\rho} v_2^2 + 2\rho_2 \hat{v} v_2 + \hat{p} \\ \hat{\rho} v_2 w_2 + \rho_2 \hat{v} w_2 + \rho_2 v_2 \hat{w} \\ (e_2 + p_2) \hat{v} + v_2 (\hat{e} + \hat{p}) \end{bmatrix}, \quad (22)$$

where \hat{e} is

$$\hat{e} = \frac{\hat{p}}{(\gamma-1)} + \frac{(u_2^2 + v_2^2 + w_2^2)}{2} \hat{\rho} + \rho_2 (u_2 \hat{u} + v_2 \hat{v} + w_2 \hat{w}). \quad (23)$$

Equation (19) has seven unknowns $f', \rho' u', v', p', T', w'$ with only five equations. The equation of state provides one more equation for ρ', p', T' , that is

$$\hat{\rho} = \gamma M_\infty^2 \frac{\hat{p}}{T} - \frac{\hat{T}}{T^2} \quad (24)$$

The last equation comes from the normal momentum equation at the upper boundary. Other equations just behind the shock was also tested but no noticeable impact on the results was observed.

E. Temporal and spatial global linear stability problems

The homogeneous equation system (11) along with proper boundary conditions form an eigenvalue problem. When a temporal linear stability problem is considered, a set of real-value α and β is given, ω is solved for as an eigenvalue problem given by Eqs. (11) and (13):

$$\omega = \omega(\alpha, \beta, Re, M_\infty). \quad (25)$$

Meanwhile, The amplitude of the disturbance modes, $[\hat{u}(y), \hat{v}(y), \hat{p}(y), \hat{T}(y), \hat{w}(y)]^{tr}$, is solved as an eigenfunction of the boundary value problem. The real part of ω , $Re\{\omega\}$, represents the frequency of the disturbance modes, while the imaginary part, $Im\{\omega\}$, represents the temporal amplification rate of the disturbances. When $Im\{\omega\}$ is greater, equal to, or smaller

than 0, a disturbance mode is unstable with finite amplification, neutrally stable, or stable with finite damping, respectively. We also define a complex wave (phase) velocity c of the disturbance waves as $c = \omega/\alpha$. The disturbance waves are three dimensional in general. Two-dimensional disturbance modes correspond to a special case of $\beta = 0$.

In order to compare with the DNS results, spatial stability problem is solved in conjunction with the shock boundary conditions. In a spatial stability problem, real-valued ω and β are assumed. While α is the complex eigenvalue to be solved for. The real part of α , α_r , represents the spatial frequency of the disturbance modes, while the imaginary part, α_i , represents the spatial amplification rate of the disturbances. When $-\alpha_i$ is greater, equal to, or smaller than 0, a disturbance mode is unstable with finite amplification, neutrally stable, or stable with finite damping, respectively.

Two linear stability numerical codes have been developed, one uses the fourth-order finite-difference discretization method, and the other uses the spectral collocation discretization methods. The detailed descriptions of these two methods can be found in Hu *et al.*,^[42] and will not be repeated here. Both methods are global eigenvalue methods providing all possible eigenmodes. Both methods can be used to solve for either the temporal or the spatial eigenvalue problems. For the temporal stability problem, discretizing Eq. (11) using the fourth-order finite-difference method or the spectral collocation method, along with the proper boundary conditions, leads to a matrix eigenvalue problem:

$$\mathbf{A}'\Phi = \omega \mathbf{B}'\Phi, \quad (26)$$

where ω is the eigenvalue. The whole eigenvalue spectrum and eigenfunctions can be obtained numerically by solving Eq. (26) using the QZ or QR eigenvalue algorithm of the IMSL computer subroutine library.

The spatial eigenvalue problem is nonlinear in the linear stability equation Eq. (11) due to the viscous \hat{u}_{xx} terms. Malik^[37] has shown that the spatial problem can be fairly accurately approximated by dropping the α^2 terms in the global eigenvalue calculations resulting a linear problem for α .

$$\mathbf{A}'\Phi = \alpha \mathbf{B}'\Phi, \quad (27)$$

More accurate spatial stability solutions can be obtained by using local iterative methods based on the global results. The spatial results shown in the follow-

ing are the global method results. Gaster's transformation

$$\alpha_i = -\frac{\partial \alpha_r}{\partial \omega_r} \omega_i \quad (28)$$

can also be used to transfer the temporal stability results to the corresponding spatial stability results.

3 DNS of Hypersonic Flow

The direct numerical simulation approach studies the transitional boundary layers^[41] by numerically solving the time-dependent three-dimensional Navier-Stokes equations for the temporally or spatially evolving instability waves. Such simulation requires that all relevant flow time and length scales are resolved by the numerical solutions using highly accurate numerical methods. One of the difficulties in hypersonic flow DNS is that high-order schemes are required for the direct simulations, however, high-order linear schemes can only be used for the spatial discretization of the equations in the flow fields without shock waves.

In Ref. [38], a new high-order (fifth and sixth order) upwind finite difference shock fitting method for the direct simulation of hypersonic flow with a strong bow shock and with stiff source terms is presented. There are three main aspects of the new method for hypersonic flow DNS: a new shock fitting formulation, new upwind high-order finite difference schemes, and third-order semi-implicit Runge-Kutta schemes recently derived^[40]. The review of other current DNS works, the details of the new method, and the results of evaluation of numerical accuracy of the new schemes can be found in Ref. [38].

The receptivity of hypersonic flows to free stream acoustic waves is investigated here. In general, three dimensional unsteady flow should be considered in the DNS studies since the most unstable first mode in hypersonic boundary layers are oblique three-dimensional instability waves^[6], though the most unstable second mode is two dimensional. Presently, only the two-dimensional instability waves in hypersonic boundary layers are considered as a first step of the DNS of three-dimensional hypersonic boundary layers over blunt bodies. The free stream disturbances are planar acoustic waves with a fixed frequency, and the body is a parabolic leading edge. The generation of disturbance waves in the boundary layer are studied based on the DNS results. The numerical accuracy of the DNS results for such hypersonic boundary layer receptivity have been evaluated by grid refinement studies

and have been reported in Ref. [38]. These test results are not presented here. The detailed results and discussion regarding DNS can be found in Ref. [38]

4 Validation of LST Results

The two linear stability codes using the fourth-order finite-difference method and the spectral collocation method were first validated by comparing their solutions with those of Malik^[37] for the linear stability of the flat-plate compressible boundary layer. Malik^[37] tested various numerical schemes for solving the temporal and spatial boundary layer linear stability problem in five test cases. The comparison of the present results with Malik's results for these five test cases are similar. The details of the comparisons can be found in [42].

The numerical codes have been used for the linear stability computations of compressible Couette flow, where the solutions of present methods were validated first by comparing with the viscous solutions of Duck *et al.*^[36] for a case of relatively low Mach number and low Reynolds numbers and then by comparing with the direct numerical simulation results by Zhong.^[38]

For the hypersonic parabolic body case, a grid refinement study is done at one station with 120 and 240 grid points. Figure 3 shows the eigenvalue spectra at one station using different number of grid points. Visual comparison shows the convergence of the stability results. A description of conditions of the hypersonic parabolic body flow will be given in the results and discussion part. The resolved least stable shock modes at station 11 are compared. The relative errors in resolving α_r and α_i are 10^{-9} and 10^{-6} respectively.

Gaster's transformation is also used to ensure the accuracy of both the temporal and spatial code. Since the spatial code solves for all the eigenvalues α_r, α_i for a given real ω , and the temporal code solves for all the eigenvalues ω_r, ω_i for a given real α , one can take one specific spatial mode (the least stable mode in this case) from the spatial eigenvalue spectrum and use the real part of the mode as the α for the temporal code to see if a corresponding least mode is resolved by the temporal code or vice versa. As a result, the ω_r reproduced from the temporal code is in very good agreement with the initial input ω in the spatial code. The relative error is 2.44×10^{-4} . The use of Gaster transformation Eq. (28) gives first order agreement between the spatial and the temporal code. This is reasonable because that Gaster's transformation is only a first order approximation.

5 Results

5.1 Flow conditions

The receptivity of a two-dimensional boundary layer to weak freestream acoustic disturbance waves for a Mach 15 hypersonic flow past a parabolic leading edge at zero angle of attack are considered. In the DNS simulation, the freestream disturbances with fixed frequencies are superimposed on the steady basic flow to investigate the development of waves in the boundary layer with the effects of the bow shock interaction. The body surface is a parabola given by

$$x^* = b^*y^{*2} - d^*, \quad (29)$$

where b^* is a given constant and d^* is the reference length. The body surface is assumed to be a non-slip wall with an isothermal wall temperature T_w^* . The free stream flow conditions are:

$$\begin{aligned} M_f &= 15, T_f^* = 192.989K, T_w^* = 1000K, \\ T_r^* &= 288K, b^* = 40m^{-1}, d^* = 0.1m, \\ \mu^* &= 0.1784 \times 10^{-4}kg/ms, \\ Re_f &= \rho_\infty^* U_f^* d^* / \mu_f^* = 6026.55. \end{aligned} \quad (30)$$

Note that low Reynolds numbers are chosen so that effective DNS simulations can be conducted. The linear stability analysis shares the same basic flow solutions with the DNS simulation. Since the linear stability analysis has to be conducted station by station, the nondimensionalization is done with respect to local shock layer edge values. The Reynolds number used in the calculations is the local Reynolds number based on the local length scale. A more standard length scale $\delta(s)$ is used to scale the resolved wave numbers and frequencies. $\delta(s)$ is defined as

$$\delta = \sqrt{\frac{s\nu_e}{U_e}} \quad (31)$$

where s is the distance from the leading edge. The Reynolds number based on this length scale δ is R . A list of local flow parameters corresponding to the station number and s coordinates are given in Table 1. Figure 1 shows the computational grids and the basic flow solutions for the velocity vectors.

5.2 LST and DNS comparisons

Due to the local nature of LST, comparisons of the disturbance eigenfunctions between LST and DNS results have to be made locally at each stations. The common forcing frequency in DNS is enforced locally at each stations in the linear stability analysis. The forcing frequencies used in the DNS and LST are $\omega_0 = 668247s^{-1}$, and $0.2\omega_0$. For the high forcing frequency case, the corresponding spatial frequency is also relatively high. The linear stability analysis is conducted over the first 11 stations. For $\omega = 0.2 \times \omega_0$ case, the corresponding spatial frequency is also low. The observed stability features from the DNS and LST take place in a much longer range in the streamwise direction. Therefore, the linear stability analysis is conducted over all 30 stations. In both cases, DNS and LST all predict distinctive wave features in the boundary layer and the shock layer. The wave features in the shock layer are relatively new and are still under investigation. The stability characteristics in the boundary layer resolved using both approaches agree with the compressible boundary layer LST predictions by Mack [4].

A. Mode structure and identification

The pressure and velocity disturbance p' and u' are chosen to be the parameter of comparison for convenience (other parameters can also be chosen as well). The pressure disturbance field, $Re\hat{p}$ and $|\hat{p}|$, resolved by DNS is shown in Fig. 2 for the $\omega = \omega_0$ case, where wave patterns are shown in contours. It is evident from the disturbance field shown that there are at least two distinctive wave patterns in the flow field. One pattern matches with the boundary layer modes which originate from the boundary layer and propagate along the wall. The other pattern is quite new and represent wave propagation close to the bow shock. Note that the waves propagating close to the shock wave form certain angles with respect to the body surface.

The eigenvalues and eigenfunctions of the disturbances at each stations are the LST results. The results for $\omega = \omega_0$ case are presented first in comparison with the DNS results as shown in Fig.2. Figure. 3 shows the spatial eigenvalue spectrum at station 11. Other spectra are similar. There are three most important modes in the flow field based on the amplification rates. Their associated amplification rate α_i are shown in Fig.4 against the local Reynolds number R . Although an accurate evaluation of the spatial frequency α_r from the DNS results is not yet available, a simple estimate of the DNS result in Fig. 2 give qualitative matches of the spatial frequencies between the DNS

results and those of the least stable modes resolved by LST.

The eigenfunctions of the most important modes are examined and compared to the disturbance profiles from DNS at various stations. The comparisons are shown in Fig. 5. Unlike the simple flat plate boundary layer case, it is found that the least stable mode at each station corresponds to a wave active in the shock layer. We will name this mode shock mode for convenience. At the early stations, the pressure disturbance of the shock mode still has finite amplitude in the boundary layer. However, it dies out downstreams and the mode remain active only close to the shock. Another interesting character of the shock mode is that its spatial frequency is almost constant (around $160m^{-1}$) in the streamwise direction matching the wave patterns observed in the DNS results. Boundary layer modes are also found by LST. They correspond to the wave features predicted close to the wall. For the $\omega = \omega_0$ case, the first modes have higher α_r and are located to the immediate right of the shock modes in the eigenvalue spectra. The second and higher modes are on the left branch of modes following the first modes.

The main character of these modes is that the pressure disturbance of these modes match with the descriptions from the compressible linear stability theory, that is, as the mode number goes higher, there are more crossing points in the pressure eigenfunction profile. It is observed from Fig.4 and the pressure eigenfunctions at each stations that initially the dominant boundary layer mode is the boundary layer first mode. This first mode is damped and the second mode takes over at around station 7. The eigenfunctions of the boundary layer second mode resolved by LST match closely with their DNS counterparts in the boundary layer at stations 9. At station 11, the third mode eigenfunction offers a closer match to the DNS results although the second mode amplification rate is slightly higher. This may imply that the second modes died out faster than predicted by LST. The match in the region close to the stagnation point is not good. In this region, LST predicts that the damped first modes are dominant. While the DNS results show that the first mode is amplified first and than stabilized. Furthermore, from the eigenfunction comparisons, the match between the first mode eigenfunctions and the DNS disturbance amplitude are not as good as that in the downstream. These discrepancies in the stagnation region are not unexpected. In the boundary layer receptivity experiments the leading edge region always see the grow of disturbance waves, and the LST prediction is only good downstream of this region. Another source of error may be the effect of curvature which is not yet accounted for by the linear stability codes. Interest-

ingly, at station 1, the eigenfunction of the shock mode bear close resemblance with the DNS disturbance amplitude. This resemblance can be further illustrated by comparing the wave patterns shown in Figs. 6 and 7. The wave patterns for each modes represented by the contours of the real part of instantaneous pressure disturbance $Re\{p'\}$ extended over one spatial period comparing with their DNS analogs provides more insights to the stability characteristics of the flow. The comparisons of the wave patterns resolved by DNS and LST at station 1 and 11 are shown in Figs. 6, and 7. It is evident that the wave patterns from both approaches match closely at station 1. Further downstream, at station 11, the shock mode wave patterns are similar to the DNS results in the shock layer, while the wave patterns of the boundary layer third mode offers close matches to the DNS wave patterns in the boundary layer.

In essence, the LST and DST predict the change of dominance from the first mode to second and higher modes along the streamwise direction in the boundary layer region. This change of dominant modes inside the boundary layer is expected. According to the boundary layer linear stability theory, when Mach number is greater than about 4 to 7, the second mode replaces the first mode to be the dominant instability. Both the first and second modes in the boundary layer are stable due to the low Reynolds number and high forcing frequency used for the flow.

For the case of $\omega = 0.2 \times \omega_0$, the evolutions of first modes, second and higher modes take place in a much longer region in the streamwise direction. In the mean time, the development of the boundary layer modes in the normal direction is affected by the shock. For example, for the second mode, the second peak of the eigenfunction happens in the shock layer. Therefore, the second and higher modes can communicate between the shock layer and boundary layer. The amplification rate path of the most important modes for the $\omega = 0.2\omega_0$ case is shown in Fig. 8. Similar to the previous case, boundary layer modes evolve from first to second modes, and even higher modes. The major difference here is that under this forcing frequency and higher Reynolds numbers down stream, the first mode wave is unstable over some distance. The second mode then takes over when the first mode is damped. DNS results predict the same trend except that the first mode is unstable for a longer distance downstreams than predicted by LST.

Figures. 9 and 10 show the velocity and pressure eigenfunctions of the first modes at station 25 and 29 comparing with the DNS results. The comparisons indicate that both methods resolve the first mode eigen-

functions in the boundary layer well. Although the linear stability theory predicts that the second mode should dominate at station 29, the DNS results show that the dominant mode is still the first mode at that station. LST also predicts shock modes may be responsible for that the wave features beyond the boundary layer resolved by DNS. In fact, the shock modes are always present and generally close to neutral. The eigenfunctions of these modes show that amplitude of these waves in the boundary layer dies down quickly downstreams. Therefore, they are not the dominant instability in the flow field. Since the DNS disturbance amplitude profile close to the shock indicate that there is another mode besides the boundary layer mode. One might speculate that the overall DNS disturbance amplitude may due to a combination of the dominant boundary layer modes, the shock modes, and the non-linear or curvature effects. This may lead to an explanation for the longer growth distance of the first mode downstreams predicted by DNS. That is, the interaction between the boundary layer mode and the wave modes originate from the shock layer extends the growth distance of the boundary layer mode. This effect can't be resolved using linear stability analysis. Stability characteristics of the unstable first mode and the second mode are studied in the next sessions.

B. Stability characteristics

It has been shown so far that both LST and DNS resolve first modes, second and higher modes in the boundary layer region. However, whether the stability characteristics of these modes are modified under the current flow conditions are not yet known. Specifically, the effects of wave angle and forcing frequency on the boundary layer modes are of interest. The effects of wave angle are studied under the temporal stability context, where wave angle is specified as $\tan(\frac{\beta}{\alpha})$, and the temporal growth rate ω_i is to be solved. Since the temporal and spatial modes under the same conditions correspond to each other, the same characteristics are expected for the spatial case. Figure 11 shows the change of frequency ω_r with wave angle for the first, second and the shock modes at station 13. It is clear that the wave angles have the same effect on the frequencies of all the modes. That is, the increase of the wave angles lowers the frequency for all the modes. Based upon the response of ω_i on the increase of wave angle, one sees from Figures 12, 13, and 14 that the first modes and the shock modes are 3-dimensional, while the second modes are 2-dimensional. These results are consistent with the compressible linear stability theory. Therefore they serve as a further confirmation of the boundary layer modes resolved.

The effects of forcing frequency has been somewhat

shown while comparing the results with ω_0 and $0.2\omega_0$. It is studied further due to its importance. There are two ways of illustrate the forcing effects. One is to fix a forcing frequency and follow the amplification rate of the least stable modes downstreams. The other is to vary the forcing frequency from ω_0 at fixed locations. Figure 15 show the amplification rate path of the first modes for $0.1\omega_0$, $0.2\omega_0$ and $0.3\omega_0$. It is clear that reducing the forcing frequency prolongs the distance of growth for the first modes. However, the Reynolds numbers at which the first modes become unstable is bigger for $0.1\omega_0$. For $0.3\omega_0$ or higher forcing frequencies, LST predicts stable first modes. Figure 16 show the amplification rates of the least stable boundary layer modes over a range of frequencies at station 13. It is shown previously that for small forcing frequencies, the corresponding spatial frequencies are also small. Therefore, at a fixed station, when the forcing frequency is reduced, lower and lower modes will dominate. The discontinuities on the α_r curves in Fig. 16 are the indications of the change of modes. The different valleys of α_i curves thus corresponds to the frequencies at which these modes are most amplified. When frequencies are high, the flow is stable since the higher modes are more stable than the lower modes. At the low frequencies, lower modes have higher amplification rates. So it is expected that this hypersonic parabolic leading edge will be more unstable with low forcing frequencies.

C. Effects of shock boundary conditions

A major effect of using shock jump conditions is that it captures the shock modes which are not resolved using the homogeneous boundary conditions. Since shock wave modes are observed in the DNS and experimental results^[50], the use of the shock jump conditions are justified. Furthermore, the eigenfunctions in the shock layer resolved using the shock conditions agree better with the DNS results. The basic features of the wave modes in the boundary layer remains the same. This is shown in Fig. 17 where the third mode gives the closest match to the DNS results. Additional shock modes may be involved for the disturbance amplitude at the shock layer. Finally, the effects of the shock jump conditions on the amplification rate of the boundary layer modes is shown in Fig. 18. Since the DNS results predicts a longer distance of spatial instability for the first modes at $\omega = 0.2 \times \omega_0$, the use of shock jump conditions provides a better prediction than the use of homogeneous boundary conditions.

6 Conclusion

Comparisons of the stability results from LST and DNS are made for the hypersonic parabolic body flow. It is shown that the LST provides individual wave modes with close resemblances to parts of the DNS solutions. In essence, the LST provides the important wave elements to the overall disturbance field captured by DNS. Specifically, these elements include the shock modes, the boundary layer first modes, second and higher modes. It is shown that the eigenfunctions of the boundary layer modes match closely with the DNS results in the boundary layer region. In the shock layer region, a combination of shock modes and the boundary layer modes may give a close match with the DNS simulation. However, perfect match is not expected at this stage due to the limitations the linear stability approach has. The effects of wave angle are studied for the important modes. The first boundary layer modes are found to be most unstable when they are three-dimensional, and the second modes are two-dimensional. This matches with the compressible linear stability theory. The shock modes are three dimensional. The effects of frequency on the important modes in the flow are studied. For ω greater than about $0.3\omega_0$, the first modes are always stable in the flow region studied. Below it, smaller frequency will increase the critical Reynolds number for the first modes but extend the growth distance. Lower forcing frequencies are found to cause instability in the flow. The linear stability analysis also shows that there are shock modes in addition to boundary layer modes. The eigenfunctions of these modes comparing with the DNS disturbance amplitude show that they consist the wave modes captured in the shock layer region by DNS.

7 Acknowledgements

This research was supported by the Air Force Office of Scientific Research under grant numbers F49620-97-10030 and F49620-95-1-0405 monitored by Dr. Len Sakell.

References

- [1] L. Lees and C. C. Lin, "Investigation of the stability of the laminar boundary layer in a compressible fluid," NACA Tech. Note 1115, 1993.
- [2] L. M. Mack, "Computation of the stability of the laminar compressible boundary layer," in *Methods*

in Computational Physics, edited by B. Adler, S. Fernbach, M. Rotenberg, Academic, 1965, pp. 247-299.

- [3] A. R. Wazzan, T. T. Okamura, and A. M. O. Smith, "Spatial and temporal stability charts for the Falkner-Skan boundary-layer profiles," McDonnell-Douglas Aircraft Co., Rept. No. DAC-67086, 1968.
- [4] L. M. Mack, "Boundary-layer linear stability theory," AGARD Rep. 704, 3-1, 1984.
- [5] M. R. Malik and S. A. Orzag, "Efficient computation of the stability of three-dimensional compressible boundary layers," AIAA paper No. 81-1277, 1981.
- [6] L. M. Mack, "Linear stability theory and the problem of supersonic boundary-layer transition," AIAA Journal, 13(3), 278-289 (1975).
- [7] J. M. Kendall, "Wind tunnel experiments relating to supersonic and hypersonic boundary layer transition," AIAA Journal, 13(3), 290-299 (1975).
- [8] A. Demetriades, "Laminar boundary layer stability measurements at Mach 7 including wall temperature effects," AFOSR-TR-77-1311, Nov. (1977).
- [9] K. F. Stetson, E. R. Donaldson, J. C. Donaldson, L. G. Siler, "Laminar boundary layer stability experiments on a cone at Mach 8, Part 2: blunt cone," AIAA paper No. 84-0006, January 1984.
- [10] M. R. Malik, R. E. Spall, C.-L. Chang, "Effects of nose bluntness on boundary layer stability and transition," AIAA paper No. 90-1112, January 1990.
- [11] E. Reshotko, M. M. S. Khan, "Stability of the laminar boundary layer on a blunted plate in supersonic flow," presented at IUTAM Symposium on Laminar-Turbulent Transition, Stuttgart, F.R.G., Sept 1979.
- [12] E. Kufner, U. Dallmann, J. Stilla, "Instability of hypersonic flow past blunt cones - effects of mean flow variations," AIAA paper No. 93-2983, January 1993.
- [13] V. Esfahanian, "Computation and stability analysis of laminar flow over a blunt cone in hypersonic flow," Dissertation Ohio State University, 1991.
- [14] L. M. Mack, "Review of linear compressible stability theory," in *Stability of Time Dependent and Spatially Varying Flows*, edited by D. L. Dwoyer and M. Y. Hussaini, Springer-Verlag, 1987, pp. 164-187.

- [15] L. M. Mack, "On the inviscid acoustic-mode instability of supersonic shear flows, part 1: two-dimensional waves," *Theoretical and Computational Fluid Dynamics*, 2, 97-123 (1990).
- [16] A. E. Gill, "Instabilities of "top-hat" jets and wakes in compressible fluids," *Physics of Fluids*, 8(8), 1428-1430 (1989).
- [17] C. K. W. Tam and F. Q. Hu, "On the three families of instability waves of high-speed jets," *Journal of Fluid Mechanics*, 201, 447-483 (1989).
- [18] M. G. Macaraeg and C. L. Street, "New instability modes for bounded, free shear flows," *Physics of Fluids*, 8(1), 1305-1307 (1989).
- [19] M. G. Macaraeg and C. L. Street, "Linear stability of high-speed mixing layers," *Applied Numerical Mathematics*, 7, 93-127 (1991).
- [20] C. K. W. Tam and F. Q. Hu, "The instability and acoustic wave modes of supersonic mixing layers inside a rectangular channel," *Journal of Fluid Mechanics*, 203, 51-76 (1989).
- [21] J. A. Greenough, J. J. Riley, M. Soetrisno, and D. S. Eberhardt, "The effects of walls on a compressible mixing layer," AIAA paper 89-0372, 1989.
- [22] M. Zhuang, P. E. Dimotakis, and T. Kubota, "The effect of wall on a spatially growing supersonic shear layer," *Physics of Fluids A*, 2(4), 599-604 (1990).
- [23] P. G. Drazin and W. H. Reid, *Hydrodynamic Stability*, Cambridge University Press, 1981.
- [24] L. A. Dikii, "On the stability of plane-parallel Couette flow," *Journal of Appl. Math. Mech.*, 29, 1009-12 (1965).
- [25] A. P. Gallagher and A. McD. Mercer, "On the behavior of small disturbances in plane Couette flow," *Journal of Fluid Mechanics*, 13, 91-100 (1962).
- [26] J. W. Deardroff, "On the stability of viscous plane Couette flow," *Journal of Fluid Mechanics*, 15, 623-31 (1963).
- [27] A. P. Gallagher and A. McD. Mercer, "On the behavior of small disturbances in plane Couette flow, part 2: the higher eigenvalues," *Journal of Fluid Mechanics*, 18, 350-2 (1964).
- [28] A. Davey, "On the stability of plane Couette flow to infinitesimal disturbances," *Journal of Fluid Mechanics*, 57(2), 369-380 (1973).
- [29] A. P. Gallagher, "On the behavior of small disturbances in plane Couette flow, part 3: the phenomenon of mode-pairing," *Journal of Fluid Mechanics*, 65, 29-32 (1974).
- [30] V. A. Romanov, "Stability of plane-parallel Couette flow," *Functional Anal. Appl.* 7, 137 (1973).
- [31] G. I. Taylor, "Fluid friction between rotating cylinder," *Proc. Royal Society London, A* 157, 546 (1989).
- [32] J. M. Robertson, "On turbulent plane-Couette flow," in *Proc. 6th Mid. Western Conf. on Fluid Mech.*, University of Texas, 169 (1959)
- [33] W. Glatzel, "Sonic instability in supersonic shear flows," *Mon. Not. R. Astron. Soc.*, 233, 795 (1988).
- [34] W. Glatzel, "The linear stability of viscous compressible plane Couette flow," *Journal Fluid Mechanics* 202, 515 (1989).
- [35] J. J. Girard, "Study of the stability of compressible Couette flow," PhD dissertation, Washington State University, 1988.
- [36] P. M. Duck, G. Erlebacher, and M. Y. Hussaini, "On the linear stability of compressible plane Couette flow," *J. Fluid Mech.*, 258, 131-165 (1994).
- [37] M. R. Malik, "Numerical methods for hypersonic boundary layer stability," *Journal of Computational Physics*, 86,376-413 (1990).
- [38] X. Zhong, "Direct numerical simulation of hypersonic boundary layer transition over blunt leading edges, part I: A new numerical method and validation," AIAA paper 97-0755, 1997.
- [39] X. Zhong, "Direct numerical simulation of hypersonic boundary layer transition over blunt leading edges, part II: A new numerical method and validation," AIAA paper 97-0756, 1997.
- [40] X. Zhong, "Additive semi-implicit Runge-Kutta schemes for computing high-speed nonequilibrium reactive flows," *Journal of Computational Physics*, 128, 19-31 (1996).
- [41] L. Kleiser, T. A. Zang, "Numerical simulation of transition in wall-bounded shear flows," *Ann. Rev. Fluid Mech.*, 23,495-535,1991.
- [42] S. H. Hu, X. Zhong, "Linear stability of supersonic plane Couette flow," AIAA paper 97-0432, 1997.
- [43] C. L. Chang, M. R. Malik, "Effects of shock on the stability of hypersonic boundary layers," AIAA paper 90-01448, 1997.

- [44] H. S. Ribner, "Convection of a pattern of vorticity through a shock wave," NACA Rept. 1164,1954.
- [45] J. F. McKenzie, K. O. Westphal, "Interaction of linear waves with oblique shock waves," Physics of Fluids, Vol.11, No. 11, pp.2350-62, 1968.
- [46] J. C. Anyiwo, D. M. Bushnell, "Turbulence amplification in shock-wave boundary-layer interaction," AIAA Journal, Vol.20, No.7, pp.893-899,1982.
- [47] T. A. Zang, M. Y. Hussaini, and D. M. Bushnell, "Numerical computations of turbulence amplification in shock-wave interactions," AIAA Journal, Vol.22, No.1, pp.12-21,1984.
- [48] G. V. Petrov, "Stability of a thin viscous layer on a wedge in hypersonic flow of a perfect gas," in Laminar-Turbulent Transition, edited by V. V. Kozlov. Proceedings of 2nd IUTAM Symposium, Springer. 1984.
- [49] S. Cowley, P. Hall, "On the stability of hypersonic flow past a wedge," ICASE Report 88-72.,1988.
- [50] M. C. Fischer, L. M. Weinstein, "Cone transitional boundary-layer structure at $M_e = 14$," AIAA Journal, Vol.10, No.5, pp.699-701, May 1972.
- [51] H. W. Liepmann and A. Roshko, *Elements of Gas Dynamics*, California Institute of Technology, 1957.
- [52] S. C. Reddy, P. J. Schmid, and D. S. Henningson, "Pseudospectra of the Orr-Sommerfeld operator," SIAM J. Appl. Maths, 53, 15 (1993).
- [53] G. K. Stuckert, "Linear stability theory of hypersonic, chemically reacting viscous flow," PhD dissertation, Arizona State University, 1988.
- [54] H. B. Johnson, G. V. Candler "Numerical study of hypersonic boundary layer transition on a blunt body," AIAA paper 97-0554, 1997.

B_{mn}' and C_{mn}' terms, which are the extra terms resolved due to the V, V', V'' terms.

$$\begin{aligned}
 B_{11}' &= \frac{VR}{\mu T} \\
 B_{22}' &= \frac{-RV}{\mu T l_2} \\
 B_{24}' &= \frac{1}{\mu} \frac{d\mu}{dT} V' \\
 B_{33}' &= \gamma M^2 V \\
 B_{34}' &= \frac{-V}{T} \\
 B_{33}' &= \gamma M^2 V \\
 B_{42}' &= 2(\gamma - 1) M^2 P_r V' l_2 \\
 B_{43}' &= -\frac{RP_r}{\mu} (\gamma - 1) M^2 V \\
 B_{44}' &= \frac{-RP_r V}{\mu T} \\
 B_{55}' &= \frac{-RV}{\mu T} \\
 C_{13}' &= \frac{-V U' \gamma M^2 R}{\mu T} \\
 C_{14}' &= \frac{V U' R}{\mu T^2} + \frac{i\alpha}{\mu} \frac{d\mu}{dT} l_0 V' \\
 C_{22}' &= \frac{-RV'}{\mu T l_2} \\
 C_{23}' &= \frac{-\gamma M^2 R V V'}{\mu T l_2} \\
 C_{24}' &= \frac{-RV V'}{\mu T^2 l_2} + \frac{1}{\mu} \frac{d\mu}{dT} V'' + \frac{1}{\mu} \frac{d^2\mu}{dT^2} T' V' \\
 C_{33}' &= \gamma M^2 V' - \frac{\gamma M^2 V}{T} \\
 C_{34}' &= \frac{-V'}{T} + \frac{2V}{T^2} T' \\
 C_{41}' &= 2i\alpha(\gamma - 1) M^2 P_r V' l_0 \\
 C_{43}' &= \frac{-\gamma M^2 R V T'}{\mu T} \\
 C_{44}' &= \frac{-RP_r V V'}{\mu T^2} (\gamma - 1) M^2 P_r V'^2 l_2 \frac{d\mu}{dt} \frac{1}{\mu} \\
 C_{45}' &= 2i\beta(\gamma - 1) M^2 P_r V' l_0 \\
 C_{53}' &= \frac{-\gamma M^2 V W' R}{\mu T} \\
 C_{54}' &= \frac{-V W' R}{\mu T^2} + i\beta V' l_0 \frac{d\mu}{dt} \frac{1}{\mu}
 \end{aligned} \tag{32}$$

Appendix

A summary of terms added when the basic flow normal velocity V, V', V'' terms are accounted for. The matrix coefficients excluding the normal velocity terms can be found in [37]. The terms listed below are called

Table 1: Flow properties by station for hypersonic flow over parabolic body.

Station	δ	R	Shock Distance	U_e
1	0.1060285E-02	34.145498333	0.17864E-01	2900.4881
2	0.1134150E-02	41.002348016	0.21903E-01	3066.9497
3	0.1207434E-02	48.016105688	0.26279E-01	3195.7327
4	0.1281194E-02	55.296790562	0.31038E-01	3299.7828
5	0.1356168E-02	62.922465807	0.36229E-01	3386.3814
6	0.1432859E-02	70.949308595	0.41894E-01	3459.9652
7	0.1511610E-02	79.417556280	0.48074E-01	3523.4246
8	0.1592649E-02	88.355371970	0.54806E-01	3578.7519
9	0.1676125E-02	97.781544440	0.62122E-01	3627.3883
10	0.1762134E-02	107.70747220	0.70053E-01	3670.4195
11	0.1850737E-02	118.13867030	0.78626E-01	3708.6905
12	0.1922085E-02	126.67682581	0.85818E-01	3735.8289
13	0.1990920E-02	135.02017330	0.92994E-01	3759.3836
14	0.2056367E-02	143.04116600	0.100026485	3779.7092
15	0.2118879E-02	150.77592664	0.106929937	3797.4740
16	0.2178818E-02	158.25403455	0.113716309	3813.1678
17	0.2236479E-02	165.50010326	0.120395652	3827.1596
18	0.2292106E-02	172.53489603	0.126976565	3839.7324
19	0.2345903E-02	179.37613534	0.133466489	3851.1081
20	0.2398043E-02	186.03910378	0.139871914	3861.4630
21	0.2448674E-02	192.53709890	0.146198544	3870.9390
22	0.2497923E-02	198.88178336	0.152451433	3879.6524
23	0.2545901E-02	205.08345865	0.158635081	3887.6987
24	0.2592705E-02	211.15128194	0.164753519	3895.1580
25	0.2638420E-02	217.09343998	0.170810379	3902.0972
26	0.2683123E-02	222.91729005	0.176808946	3908.5733
27	0.2726880E-02	228.62947531	0.182752205	3914.6350
28	0.2769753E-02	234.23602015	0.188642877	3920.3239
29	0.2811796E-02	239.74240952	0.194483456	3925.6763
30	0.2853058E-02	245.15365556	0.200276231	3930.7235

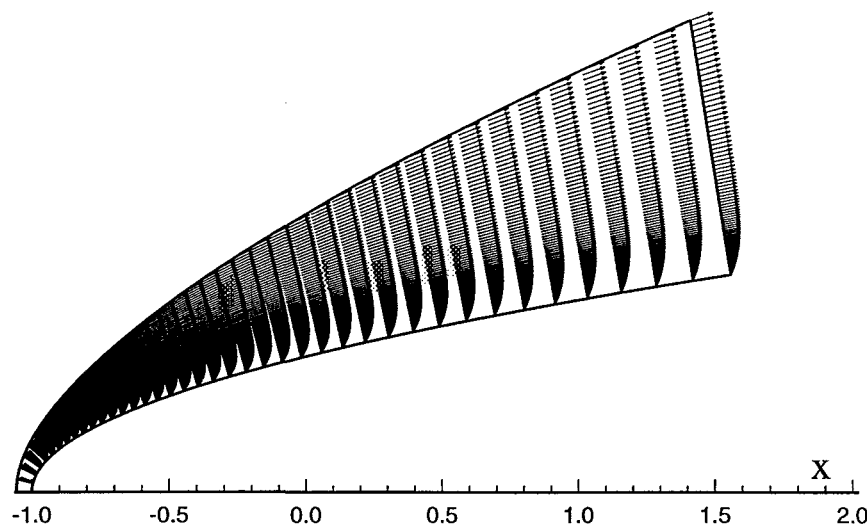
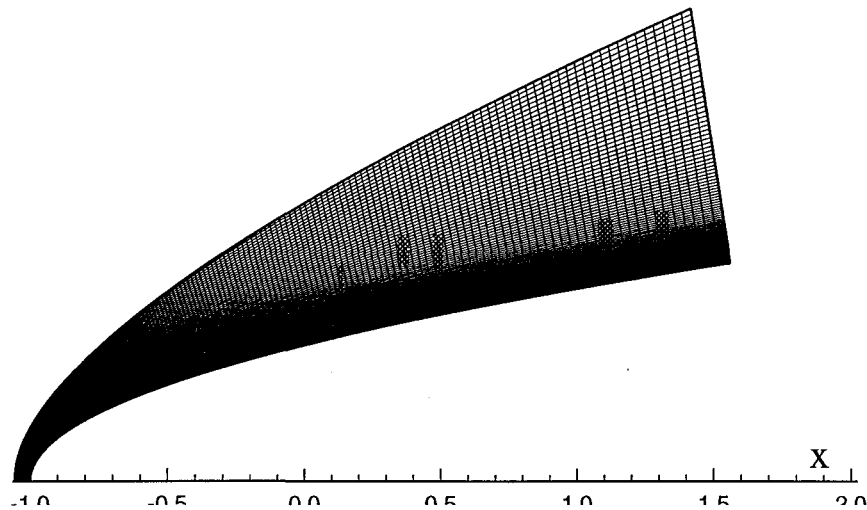


Figure 1: Basic flow solutions for computational grid (upper figure) where the bow shock shape is obtained as the numerical solution for the freestream grid line, velocity vectors for hypersonic flow over a parabolic body.

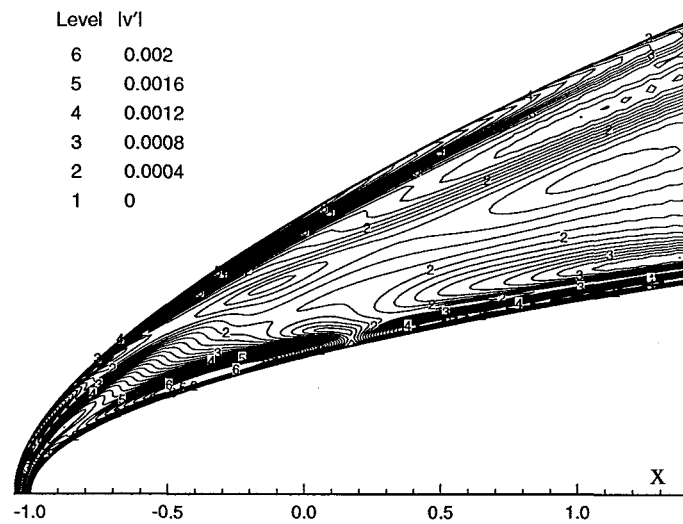
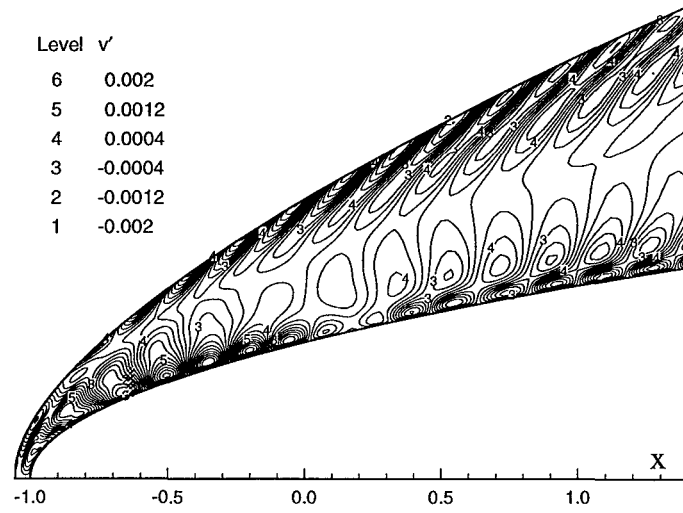


Figure 2: The DNS results of instantaneous contours: instantaneous v' (upper figure), Fourier amplitude $|v'|$ (lower figure).

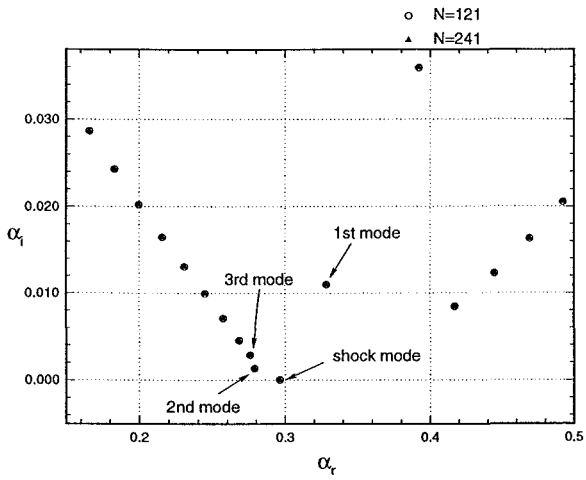


Figure 3: Spatial eigenvalue (α) spectra at station 11 resolved using 121 and 241 grid points.

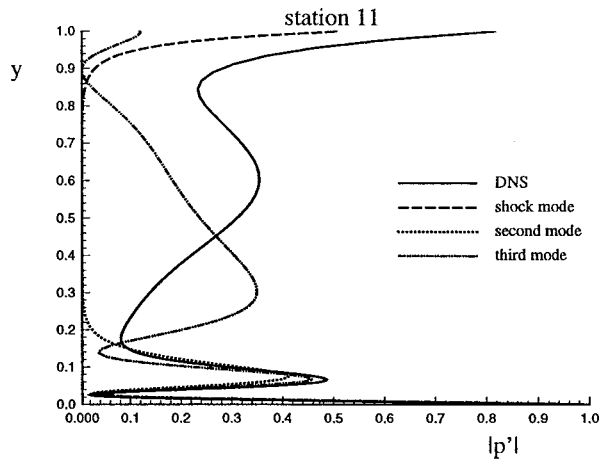
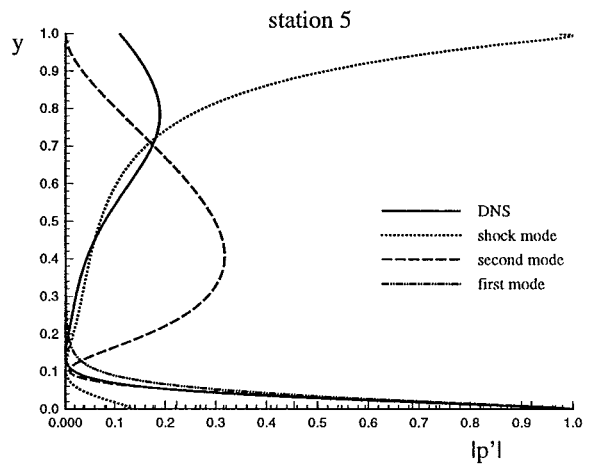
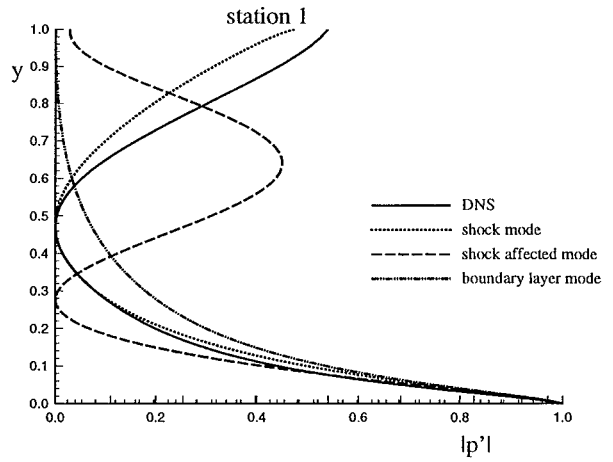


Figure 5: Spatial eigenfunctions of $|p'|$ for different modes from LST comparing to the DNS results at station 1 (upper figure), station 5 (middle figure), and station 11 (lower figure).

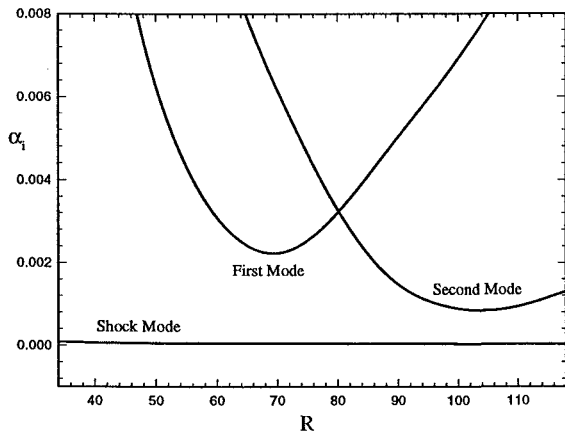


Figure 4: The amplification rate path for three different modes in the streamwise direction, $\omega = \omega_0$.

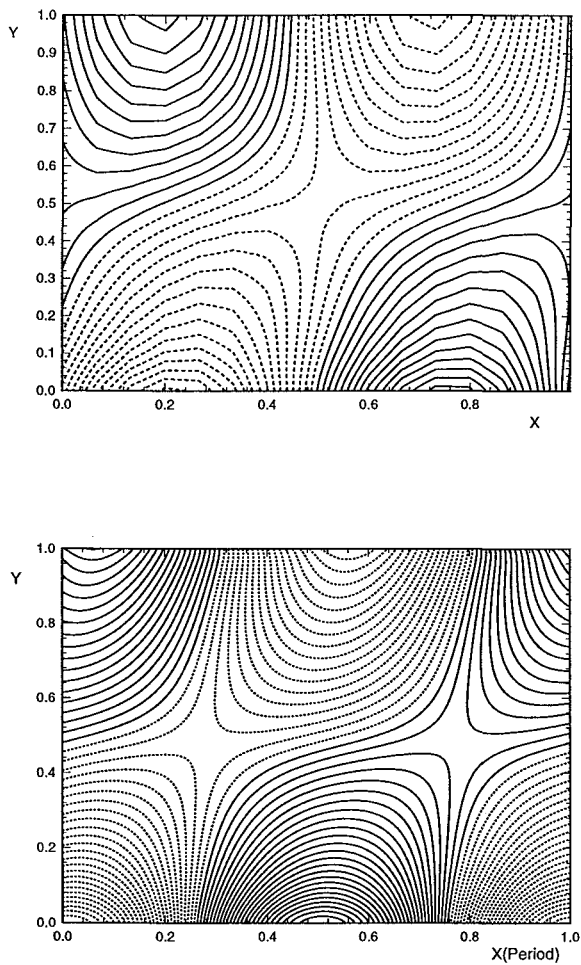


Figure 6: Wave patterns of $Re\{p'\}$ from LST (lower figure) comparing to the DNS results (upper figure) at station 1.

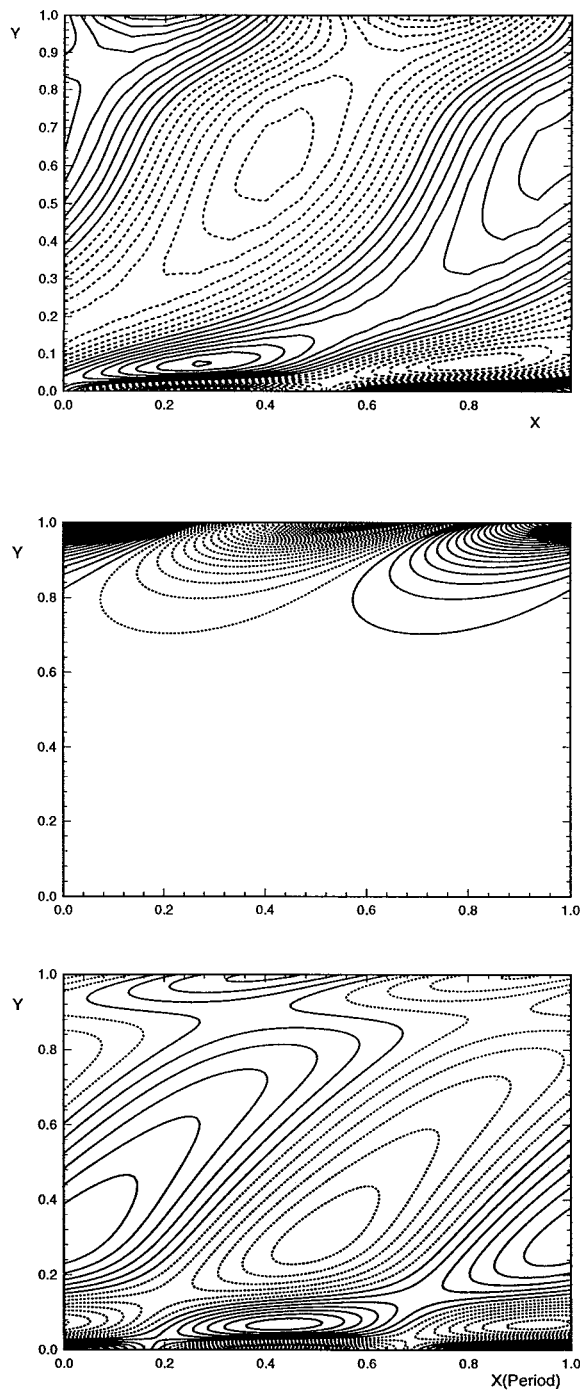


Figure 7: Wave patterns of $Re\{p'\}$ from LST comparing to the DNS results (upper figure) at station 11. The LST shock mode is shown in the middle figure, and the third mode is shown in the lower figure.

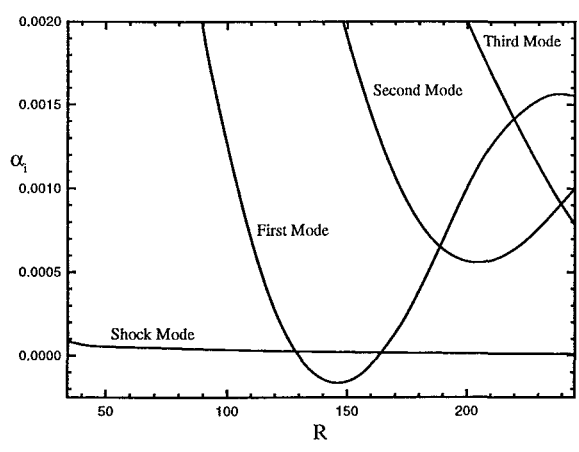


Figure 8: The amplification rate path for the three different modes in the streamwise direction.

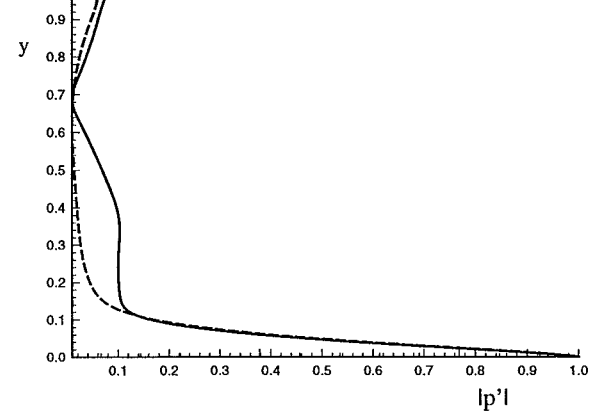
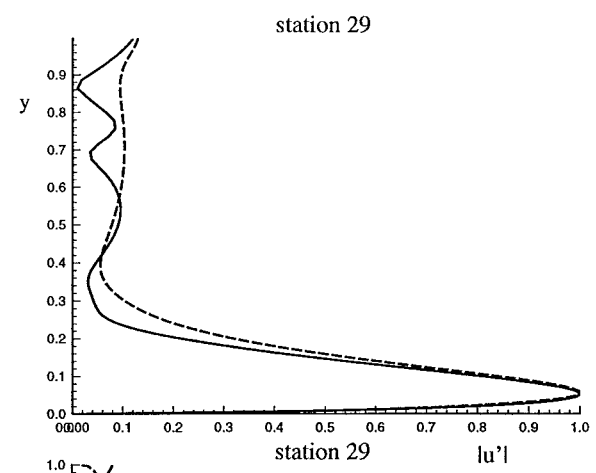


Figure 10: Eigenfunction of the first mode at station 29 comparing with the DNS disturbance amplitude. Upper figure u' , lower figure p' .

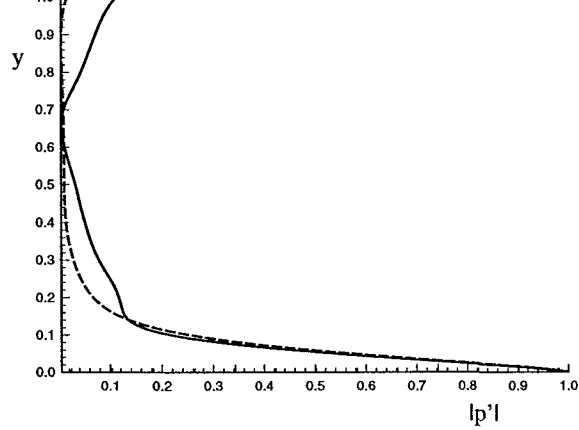
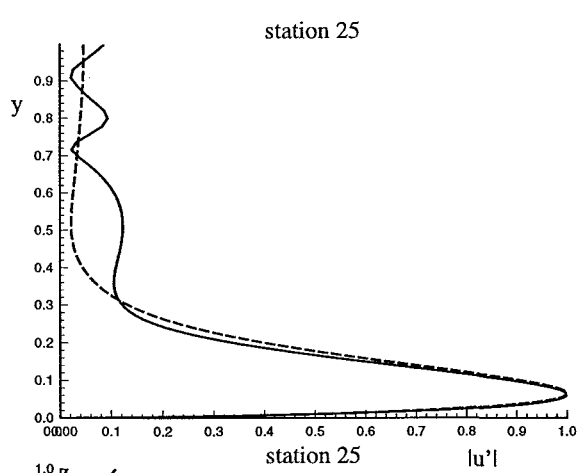


Figure 9: Eigenfunctions of the first modes at station 25 comparing with the DNS disturbance amplitude. Upper figure u' , lower figure p' .

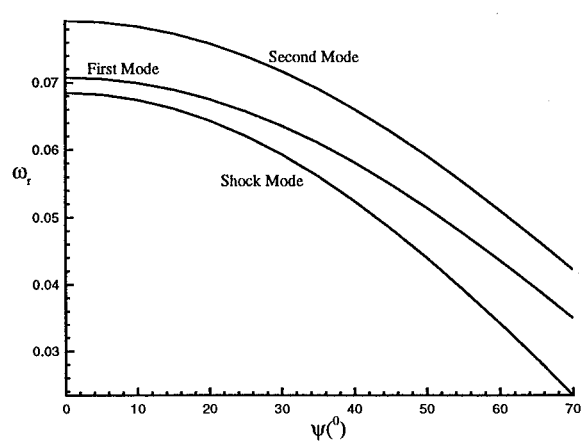


Figure 11: The change of frequency (ω_r) of the wave modes with wave angle.

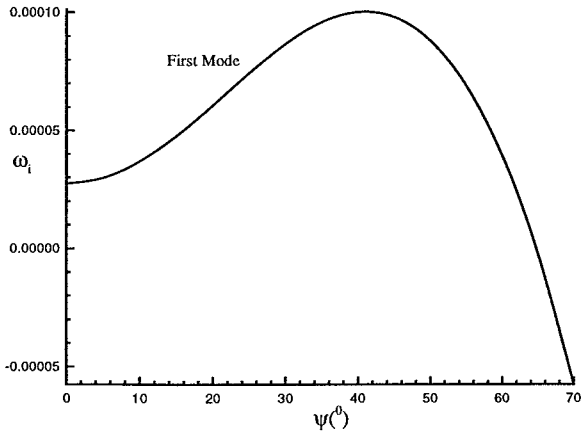


Figure 12: The change of amplification rate (ω_i) of the boundary layer first modes with wave angle.

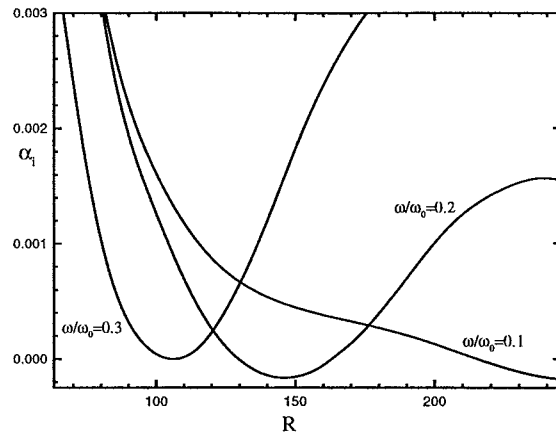


Figure 15: The amplification rate path (α_i) in the streamwise direction with various forcing frequencies for first modes.

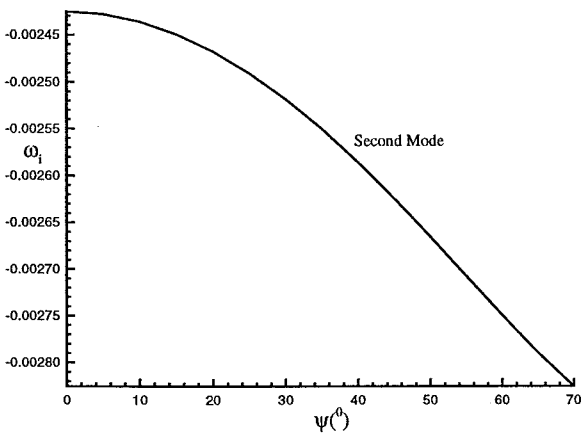


Figure 13: The change of amplification rate (ω_i) of the boundary layer second modes with wave angle.

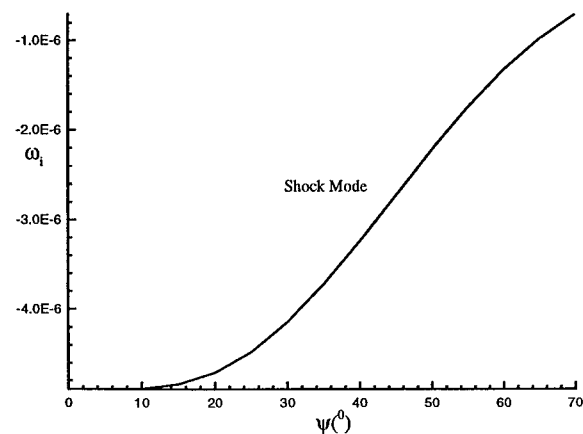


Figure 14: The change of amplification rate (ω_i) of the shock modes with wave angle.

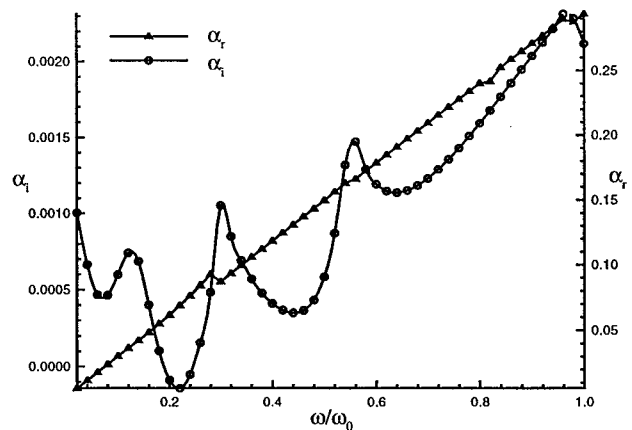


Figure 16: The maximum amplification rates (ω_i) of boundary layer modes at various frequencies at station 13.

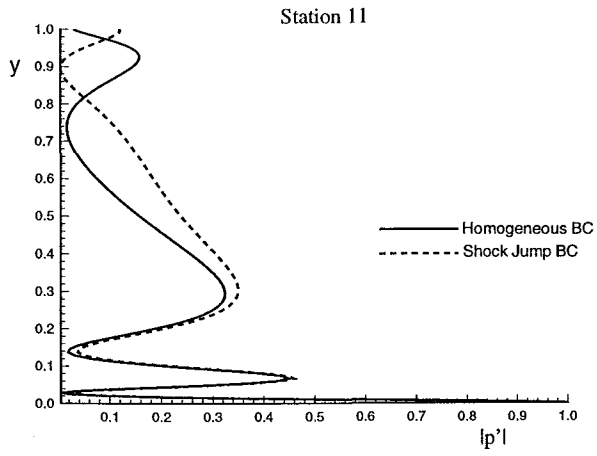


Figure 17: Pressure amplitude for the third mode at station 11 with shock conditions and homogeneous conditions.

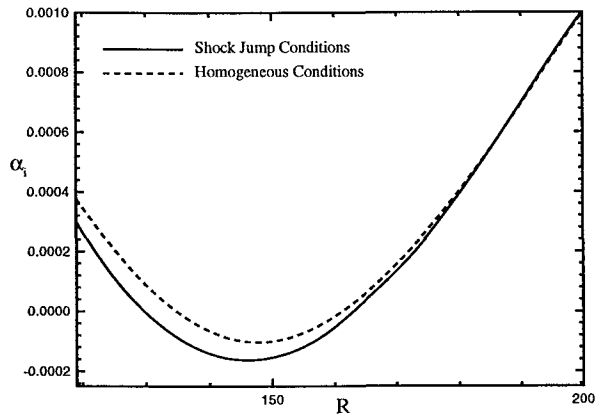


Figure 18: The amplification rates predicted by LST using shock conditions and homogeneous conditions at $0.2\omega_0$.